catalysts

MDPI

Article

Rare-Earth/Manganese Oxide-Based Composites Materials for Electrochemical Oxygen Reduction Reaction

Stefan V. Panić [1], Marijana R. Pantović Pavlović [1,2], Miroslava M. Varničić [1], Vojin Tadić [3], Srećko Stopić [4], Bernd Friedrich [4] and Miroslav M. Pavlović [1,2,*]

[1] Department of Electrochemistry, Institute of Chemistry, Technology and Metallurgy, National Institute of the Republic of Serbia, University of Belgrade, Njegoševa 12, 11000 Belgrade, Serbia; stefan.panic@ihtm.bg.ac.rs (S.V.P.); m.pantovic@ihtm.bg.ac.rs (M.R.P.P.); varnicic@ihtm.bg.ac.rs (M.M.V.)
[2] Center of Excellence in Environmental Chemistry and Engineering-ICTM, University of Belgrade, Njegoševa 12, 11000 Belgrade, Serbia
[3] Department for Experimental Testing of Precious Metals, Mining and Metallurgy Institute, Zeleni Bulevar 35, 19210 Bor, Serbia; vojintadic@yahoo.com
[4] Process Metallurgy and Metal Recycling, RWTH Aachen University, Intzestraβe 3, D52072 Aachen, Germany; sstopic@ime-aachen.de (S.S.); bfriedrich@ime-aachen.de (B.F.)
* Correspondence: mpavlovic@tmf.bg.ac.rs

Abstract: The main objective of this research was a systematic development of advanced micro/nanostructured materials based on the most used metal-oxides for ORR and metal-oxides with an extremely low-loading of Pt for comparison. Hybrid composites compared were: MnO_2, La_2O_3, mixed lanthanum manganese oxides (LMO), and mixed lanthanum manganese oxides with reduced platinum load (LMO-Pt). The influence of the reduced amount of noble metal, as well as single oxide activity toward ORR, was analyzed. The complete electrochemical performance of the hybrid materials has been performed by means of CV, LSV, and EIS. It was shown that all synthesized catalytic materials were ORR-active with noticeable reduction currents in O_2 saturated 0.1 M KOH. The ORR behavior indicated that the La_2O_3 electrode has a different mechanism than the other tested electrode materials (MnO_2, LMO, and LMO-Pt). The EIS results have revealed that the ORR reaction is of a mixed character, being electrochemically and diffusion controlled. Even more, diffusion is of mixed character due to transport of O_2 molecules and the chemical reaction of oxygen reduction. O_2 diffusion was shown to be the dominant process for MnO_2, LMO, and LMO-Pt electrolytic materials, while chemical reaction is the dominant process for La_2O_3 electrolytic materials.

Keywords: oxygen reduction; hybrid materials; manganese oxide; lanthanum oxide; Pt as catalyst; fuel cell; cathode reaction

Citation: Panić, S.V.; Pantović Pavlović, M.R.; Varničić, M.M.; Tadić, V.; Stopić, S.; Friedrich, B.; Pavlović, M.M. Rare-Earth/Manganese Oxide-Based Composites Materials for Electrochemical Oxygen Reduction Reaction. *Catalysts* **2022**, *12*, 641. https://doi.org/10.3390/catal12060641

Academic Editor: Svetlana B. Štrbac

Received: 27 May 2022
Accepted: 10 June 2022
Published: 12 June 2022

1. Introduction

Fuel cells, batteries, and supercapacitors are known as the most efficient and promising technologies for electrochemical energy conversion and storage. The main constraints for their production for practical use are primarily due to the high cost of materials, as follows: e.g., noble metals such as platinum, as well as rather poor operational stability in different climate environments. The long-lasting challenge is to provide an advanced low-cost catalyst with performance as efficient as noble metals or better. Therefore, the rational design of novel multicomponent materials with improved catalytic properties can lead to alternatives that can compete with existing technologies.

Alternative energy devices are one of the most efficient and clean energy-producing sources available [1]. Still, the sluggish kinetics of the electrochemical oxygen reduction reaction (ORR) is detected as the main limitation. Noble metals (e.g., Pt, Au) are used and considered the most efficient catalysts for their performance, but at the same time, due to their high cost and scarcity, commercialization of these energy devices is impeded [2–4].

In the last decades, the main idea has been to reduce the loading of noble metals in the electrode material but to keep the same activity that their bulk electrode provides for the desired reactions.

In particular, micro/nanomaterials with a suitable combination of the components were investigated as a promising strategy toward high-performance electrode materials. For example, transition metal oxides (TMO) such as MnO_2, Co_2O_3, etc. have been studied, due to their rich oxidation states, high specific capacitances, low cost, and environmental friendliness [5,6]. Among TMOs, the focus is mostly based on MnO_2, which is already indicated as a non-carbon material of potent catalytic activity improvements while being used as a noble metal carrier [7]. It has been reported that manganese oxide promotes oxygen disproportionation, resulting in an overall four-electron reduction of O_2 on MnOx/Nafion modified electrodes [8]. Unfortunately, the electrochemical performance of single MnO_2 electrodes is limited by poor electrical conductivity (10^{-5}–10^{-6} S cm^{-1}) [9,10]. An effective way to improve the utilization of MnO_2 is to combine conductive materials (metals, oxides, carbon-based materials) to form composites as electrode materials with improved characteristics. For example, Xia et al. have reported the fabrication of composite materials with core-shell structures of Co_2O_3@Pt@MnO_2 as high-performance electrode materials for supercapacitors [10]. Lahousse et al. have found an MnO_2/TiO_2-Pt electrocatalyst of high-measured catalytic activity in comparison to the noble metal catalysts [11]. Various combinations of mixed oxide materials have been investigated so far, e.g., 3D flower-like Co_2O_3@MnO_2 [6], nanosheets of MnO_2 [12], CuO/MnO_2 [13], NiO/MnO_2 [14], etc.

Additionally, among rare earth oxides, lanthanum oxide (La_2O_3) has been extensively analyzed for its excellent electronic, photocatalytic, and electrocatalytic properties [15,16]. It has been discovered that the existence of the interlayer defect structure of the oxides was helpful for the active oxygen adsorption and had a positive effect on catalyzing ORR [17]. On the other hand, despite its outstanding electronic structure, quite similar to MnO_2, the single oxide has low electroconductivity. Therefore, lots of effort has been put into the development of a hybrid composite material that would combine all the benefits of the metals. In this regard, perovskite oxides with an ABO_3 structure have attracted great attention as a replacement metal oxides. Various perovskites have been developed, such as $LaMnO_3$, $LaCoO_3$, $LaNiO_3$, $LaCrO_3$, and $LaFeO_3$ [18–20]. In particular, Co and Mn-based perovskites have shown high and stable performance for ORR as well as for the oxygen evolution reaction (OER). This bifunctional property is due to its oxidation states and spin configuration [21]. Recently, $LaMnO_3$ nanoparticles were found to achieve high energy and power densities, synthesized using natural lemon juice as a green surfactant [22]. However, due to various structures, a combination of metals, and the synthesis procedure reported, the systematic design and comparison of metal oxide-based electrode materials is necessary.

The main aim of this paper was a basic analysis and comparison of the lanthanum and manganese-based hybrid materials for ORR of reduced Pt loading. In addition, the utilization of cheap and stable carrier materials (e.g., TMOs) were used, which were supposed to contribute to the activity of a reduced number of noble metals.

The syntheses of hybrid electrocatalytic materials with detailed electrochemical characterization were conducted. The electrode materials based on La_2O_3/MnO_2 (LMO) have been synthesized by one-pot synthesis, and the influence of the addition of Pt low loading has been investigated. Transition metal oxides were chosen as base support due to their double-role potential, one of which was to serve as stabilizing catalyst carriers while the other one had interactive participation in the enhancement of the catalytic properties of noble metals. Electrochemical characterizations have been carried out by means of cyclic voltammetry (CV), linear sweep voltammetry (LSV), and electrochemical impedance spectroscopy (EIS) in 0.1 M KOH. ORRs were investigated in the 3-electrode set-up using a rotating disk (RDE) as a working electrode to provide controlled mass transport conditions.

2. Results and Discussion

Stable cyclic voltammograms (CVs) of La_2O_3, MnO_2, LMO, and LMO–Pt thin-layer electrodes are shown in Figure 1.

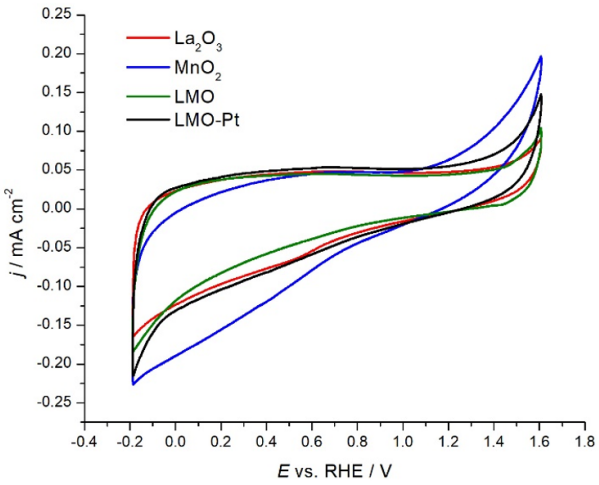

Figure 1. Stable cyclic voltammograms of La_2O_3, MnO_2, LMO, and LMO-Pt thin-layer electrodes at scan rate of 50 mV s^{-1} in N_2-saturated 0.10 M KOH at room temperature.

There are no significant differences in the La_2O_3, LMO, and LMO-Pt CV responses. MnO_2 exhibits slightly higher cathodic currents in the range from 1.0 to −0.2 V, which meets the value for LMO–Pt material at $E = -0.2$ V. For an LMO–Pt sample, the onset of the hydrogen evolution reaction is clearly visible around 0.0 V due to the presence of Pt. Although being quite weak, the broad redox pair peak around 0.6 V can be distinguished for La_2O_3, MnO_2, and LMO-Pt. The only anodic shoulder-like peak that can be distinguished for LMO.

MnO_2 cyclic voltammogram in the potential range of −0.2 V to 1.6 V in 0.10 M KOH electrolyte represents a typical voltammogram with a wide reduction peak related to the reduction reactions of MnO_2 to Mn_2O_3, Mn_3O_4, and finally to $Mn(OH)_2$. The anodic counterpart appears as the increase in currents at the potentials above 1.1 V. The broad peaks of other materials, La_2O_3, LMO, and LMO-Pt, belong to mutual redox reactions of rare earth metals and Mn oxides. These voltammograms show forms that are typical for the materials that could be associated with the pseudocapacitive response of these faradaic processes. The absence of ideal linearity and symmetry between the charge-discharge processes can be observed as wider discharge counterparts.

The prepared electrocatalytic materials were tested for their ORR activity by means of LSV in an O_2-saturated 0.10 M KOH electrolyte. Figure 2 presents the ORR electrochemical performances of La_2O_3, MnO_2, LMO, and LMO-Pt thin powder layers at the electrode rotating speed of 1000 rpm.

Noticeable reduction currents can be observed as a result of ORR. The ORR onset potential for MnO_2, LMO, and LMO-Pt electrodes was approx. 0.7 V, which is comparable to previous work [23], while the onset potential for the La_2O_3 electrode was around 0.8 V. The MnO_2, LMO, and LMO-Pt electrode materials show similar curve shapes and activity. For all of the materials, the curve appears stepped, with a transition around 0.4 V. This could also be an indication of different ORR mechanisms, with La_2O_3 electrode material being quite a different mechanism with respect to MnO_2, LMO, and LMO-Pt electrode materials. It can be noticed that LMO electrode material has a more similar behavior to La_2O_3 electrode material in the potential range from 0.3 V to −0.2 V, while the former exhibits the highest activity below ca. 0.0 V. MnO_2 and LMO-Pt have quite similar curve shapes in the mentioned potential range. The MnO_2 electrode material has the smallest ORR activity amongst three named electrodes with a current plateau of around −1.9 mA cm^{-2},

followed by LMO (-2.0 mA cm^{-2}) and, finally, LMO with 5 mass% of Pt (-2.3 mA cm^{-2}). The La_2O_3 electrode material has a different shape of polarization curve. This indicates that different ORR mechanisms could be taking place on the La_2O_3 thin layer; the ORR starts at more positive potentials and, consequently, the overpotential is lower at the potentials positive to ca. 0.65 V). This feature is similar to the ORR activity of commercial 20 mass% Pt@XC-72 catalysts [23,24]. However, the ORR current plateau is considerably lower (-1.3 mA cm^{-2}) with respect to other samples.

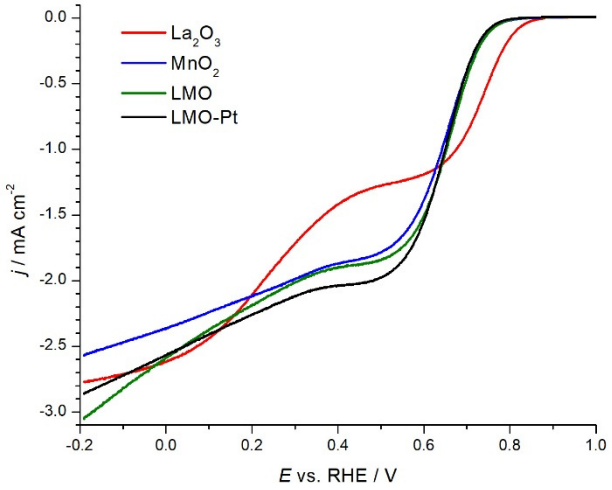

Figure 2. ORR activities of La_2O_3, MnO_2, LMO, and LMO-Pt electrode materials at the scan rate of 2 mV s^{-1} and electrode rotating speed of 1000 rpm; 0.1 M NaOH, 25 °C.

Tafel analysis is generally utilized to compare the electrocatalytic activity of the electrodes and to discriminate the reaction mechanisms of the reactions with mass transfer limitations at low to moderate overpotentials.

Ohmic-drop-compensated potentiodynamic Tafel curves for the ORR at La_2O_3, MnO_2, LMO, and LMO-Pt materials in O_2-saturated 0.10 M KOH are shown in Figure 3 (the overall current is examined since well-developed diffusion current density plateaus have not been registered to apply the typical Koutecky–Levich analysis).

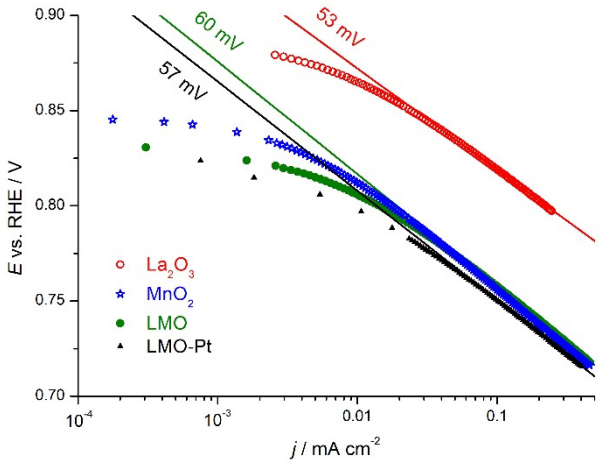

Figure 3. Ohmic-drop-compensated potentiodynamic Tafel curves for the ORR at La_2O_3, MnO_2, LMO, and LMO-Pt material in O_2-saturated 0.10 M KOH, 25 °C.

It can be seen in Figure 3 that all the electrode materials exhibit Tafel slope at low overpotentials (up to 100 mV) between 53 and 60 mV dec^{-1} (lines). Tafel analysis leads to the following two important physical parameters: the Tafel slope and the exchange

current density. Based on the theory of ORR mechanisms, the Tafel slope of 60-mV dec^{-1} determines the overall reaction rate when the surface adsorption of the species MOO and MOO− is most likely the rate-determining step [25,26]. One can observe that, in the measured overpotential range, La_2O_3 material has the highest currents. At lower overpotentials (0.8–0.9 V potential region), MnO_2 has one of the highest currents among Mn-containing samples; at higher overpotentials (at potentials negative to ca. 0.75 V), the highest ORR currents are registered for Pt-free Mn oxide-based materials. In this high-overpotential range, LMO-Pt's activity appears to approach the activities of MnO_2 and LMO. Samples are of considerably lower ORR activity than bulk Pt (the Tafel slope of 52 mV dec^{-1} was registered (not shown)). The lower activity could be attributed to the fact that there is only 5 mass% of Pt in the LMO-Pt electrolytic material, which is quite low content to induce the ORR activities close to bulk Pt. Moreover, from Figure 2, it can be seen that La_2O_3 electrolytic material loses considerably its highest low-overpotential activity and reaches the lowest limiting currents.

The current densities per mol of a metal could be a useful indication of the specific activity of the components in the composites [23]. This parameter was calculated at the potential in the region of calculated slopes of Tafel dependencies, and the results are shown in Table 1.

Table 1. The current densities per mol of a metal for La_2O_3, MnO_2, LMO, and LMO-Pt electrolytic material in O_2-saturated 0.10 M KOH.

	j_{La} (A mol^{-1})	j_{Mn} (A mol^{-1})	j_{Pt} (A mol^{-1})
La_2O_3	0.78	-	-
MnO_2	-	4.14	-
LMO	13.0	10.3	-
LMO-Pt	9.71	7.65	168.3

It can be concluded that La improves the activity of Mn at lower overpotentials but not at higher ones.

To further analyze the ORR activities and their correlation to sample structures, potentiostatic electrochemical impedance spectroscopy (PEIS) measurements were performed at open circuit potential for all the samples in an N_2-saturated 0.1 M KOH solution. Galvanostatic electrochemical impedance spectroscopy (GEIS) measurements were performed at OCP and the current from a low- to moderate-overpotential region of −0.765 mA cm^{-2} (with an amplitude of 0.510 mA cm^{-2}) for all the samples in an O_2-saturated 0.1 M KOH solution in order to evaluate the details of ORR activity and the electrochemical behavior of the tested materials.

The PEIS results, shown as the capacitance complex plane plots (CCPPs) of the synthesized materials, are given in Figure 4a. CCPPs show differences in capacitive features between the tested electrodes. The mutual characteristic is a well-resolved capacitive loop in the high-frequency domain followed by straight-line behavior in the low-frequency domain. The capacitive loop for the Pt-modified LMO electrode is of a higher diameter than LMO itself, and the highest among all of the samples, meaning the capacitance is considerably increased by Pt–modification. Samples involving single oxides–MnO_2 and La_2O_3 exhibit similar EIS features of two indicatively overlapped capacitive loops of similar diameters. The region consisting of a loop-like response at high frequencies corresponds to pseudocapacitive redox transitions of a metal ion from the oxide. The straight-line behavior in the low-frequency region is attributed to the ionic exchange in the electrolyte/material interphase.

The impedance features from Figure 4a of the investigated electrodes have been simulated by the equivalent electrical circuit (EECs). The impedance characteristics of EECs are indicated by lines in the capacitance complex plane plots of Figure 4a. Samples' PEIS responses are described by different circuits and are shown in Figure 4b–d. The framework for fitting was to quantify the EIS behavior through the simplest suitable EEC with the

lowest possible fitting error. The EECs correspond to those applied in the literature [27,28] and are typical for porous structures. EECs are presented as resistors and constant phase elements (CPEs) through the branches. The Chi-squared calculated was below 0.004, while the relative error of parameter values did not exceed 34%. The equivalent electric circuits used to fit the data gave similar fitting quality for the electrode based on LMO and MnO_2.

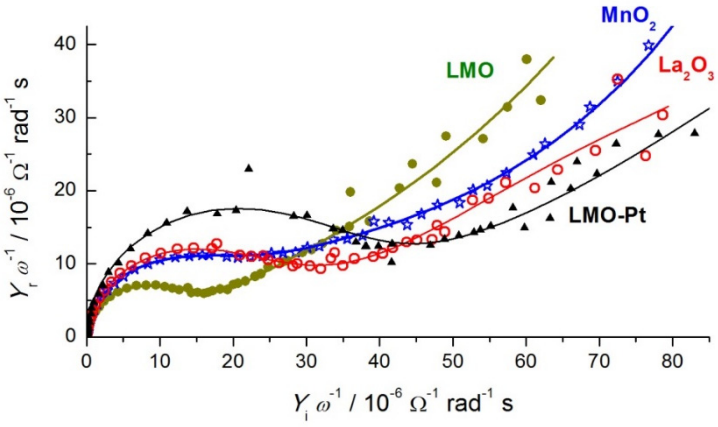

(**a**)

(**b**) La_2O_3-electrode

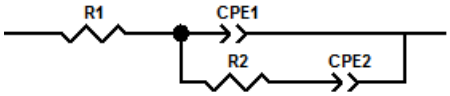

(**c**) LMO and MnO_2-electrode

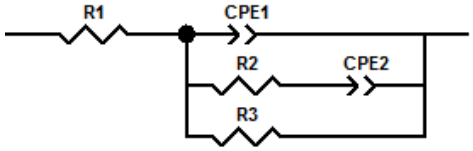

(**d**) LMO-Pt-electrode

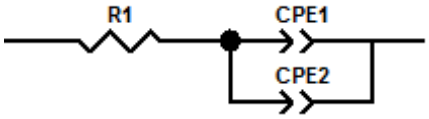

Figure 4. (**a**) Capacitance complex plane plots for synthesized materials at OCP in 0.10 M KOH and (**b**–**d**) equivalent circuits used to fit the experimental EIS data. Equivalent electric circuit data are presented by *lines* in the plots.

The results obtained for La_2O_3, MnO_2, LMO, and LMO-Pt electrolytic material in N_2-saturated 0.10 M KOH from fitting results using EECs are given in Table 2.

Table 2. Electrochemical impedance spectroscopy data for La_2O_3, MnO_2, LMO, and LMO-Pt electrocatalytic materials in N_2-saturated 0.10 M KOH gained at OCP.

	CPE1-T (μF)	CPE1-P	CPE2-T (μF)	CPE2-P	R2 (Ω)	R3 (Ω)
La_2O_3	56.7	0.86	18.9	0.635	4.89×10^4	
MnO_2	54.5	0.85	21.0	0.658	2.50×10^3	1.31×10^5
LMO	31.6	0.88	23.4	0.593	4.89×10^3	3.74×10^5
LMO-Pt	60.6	0.9	24.9	0.515		

From the results shown in Figure 4 and Table 2, one can conclude that there are two time constants. CPE1 corresponds to the capacitive response of the outer surface of the electrode materials readily available to the electrolyte, and CPE2 corresponds to the capacitive response of the inner layer surfaces that are less accessible. The R1 resistance corresponds to the solution resistance. It can be seen that R3 is present in the EEC for MnO_2 and LMO. It appears that R3 describes the feature related to MnO_2 and its redox transitions

to different oxidation states. This statement is supported by the value of R3 of LMO, in which the content of Mn is lower with respect to the pure MnO_2 layer. The R3 value of LMO is almost three times higher than the R3 value of MnO_2. If R2 is taken into consideration, the most inclined conclusion could be that it represents the redox resistance at the inner surfaces rather than the pore resistance, which should be comparatively negligible for Mn-containing samples (R2 is also higher for LMO in comparison to pure MnO_2). On the other hand, R2 could be dominated by the pore resistance in La_2O_3 due to less pronounced pseudocapacitive behavior since R3 was not required in the EEC. Consequently, R2 is an order of magnitude higher for La_2O_3 in comparison to MnO_2 and LMO. In the case of LMO-Pt, Pt causes these resistances to not affect the PEIS response.

The GEIS results for La_2O_3, MnO_2, LMO, and LMO-Pt in O_2-saturated 0.10 M KOH are shown in Figure 5.

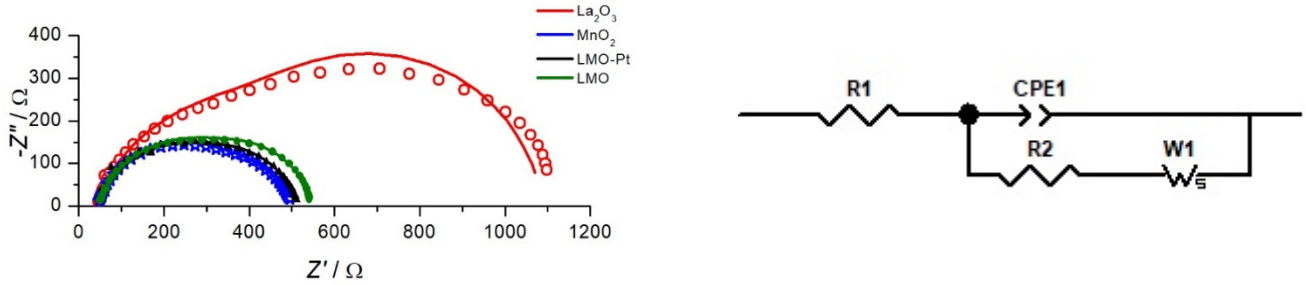

(**a**) (**b**)

Figure 5. (**a**) Nyquist diagrams of La_2O_3, MnO_2, LMO, and LMO-Pt electrocatalytic materials in O_2-saturated 0.10 M KOH at current of −0.15 mA with an amplitude of 0.10 mA and (**b**) equivalent circuits used to fit the experimental EIS data. Equivalent electric circuit data are presented by *lines* in the plots.

With an amplitude of 0.510 mA cm^{-2}, the GEIS measurements of La_2O_3 electrode material enter the limiting current region according to Figure 2. Two overlapped semicircles can be seen for all the materials. Taking the semicircle diameter as a measure of the charge transfer resistance, i.e., ORR activity, the activity series in the tested region is as follows: MnO_2 > LMO-Pt > LMO > La_2O_3. The ratio of the two more or less overlapped semicircles for the materials differs too. For LMO-Pt and MnO_2, the diameter of the high-frequency semicircle is a bit larger than that of the low-frequency one. For LMO, the two diameters are of similar values, whereas the diameter of the low-frequency semicircle is larger for La_2O_3. The ORR is of mixed limiting character, being electrochemically- and diffusion-controlled. High-frequency response corresponds to charge transfer, and low-frequency corresponds to mass transfer limitations. The authors are fond of believing, according to findings from PEIS measurements, that the limiting current for the tested materials is the consequence of the chemical character of the materials rather than mass transfer. Despite pronounced activity at low overpotentials, La_2O_3 has much larger mass transport limitations (the diameter of the low-frequency semicircle is considerably larger) in comparison to other samples. Apparently, this reflects the lowest position of the limiting current plateau of La_2O_3 from Figure 2. This most pronounced ORR limiting condition also affects the diameter of the high-frequency loop, which is not straightforwardly seen for Mn-containing samples. These features indicate that ORR at La_2O_3 is not subjected only to diffusion limitations, but to limitations related to some slow chemical reaction(s).

The fitting results gained by EEC (Figure 5b) for ORR at La_2O_3, MnO_2, LMO, and LMO-Pt are given in Table 3.

Table 3. Galvanostatic electrochemical impedance spectroscopy data for La_2O_3, MnO_2, LMO, and LMO-Pt in O_2-saturated 0.10 M KOH obtained at $I_s = -0.765$ mA cm^{-2} with an amplitude of 0.510 mA cm^{-2}.

	CPE1-T (μF)	CPE1-P	W1-R (Ω)	W1-T (s)	R1 (Ω)	R2 (Ω)
La_2O_3	128.8	0.84	18.9	0.53	43.8	518
MnO_2	167.5	0.83	69.7	0.53	45.7	376
LMO	143.7	0.83	123.3	0.301	46.7	375
LMO-Pt	149.2	0.80	82.3	0.241	43.1	386

Owing to finite diffusion of O_2, the finite length Warburg short circuit terminus was introduced (Ws). This element is also known as a Generalized Finite Warburg element (GFW), which is an extension of the Finite-Length Warburg (FLW). To allow its full finite diffusion assignment, the Ws-P parameter was fixed to 0.5. The FLW represents the solution of the one-dimensional diffusion equation of diffusion species, which is completely analogous to wave transmission in a finite-length RC transmission line. Ws-T parameter equals L^2/D, where L is the effective diffusion thickness, and D is the effective diffusion coefficient. The Ws-R parameter defines a finite resistivity to diffusion. At very low frequencies, Z′ approaches Ws-R while Z″ tends to zero.

The Warburg element is dominant in the low-frequency region. The larger the Ws-T parameter, the greater the diffusion thickness of specific species. R2 is charge transfer resistance, which shows the activity of the electrode materials towards ORR. From the results given in Table 2, GEIS shows that at measured current density, MnO_2, LMO, and LMO-Pt have almost the same activity towards ORR, while the activity of La_2O_3 is almost twice as low. The higher the resistance, the lower the activity. On the other hand, the W1-T time constant is in direct correlation with the thickness of the double layer. Table 2 shows that the effective diffusion thickness of La_2O_3 and MnO_2 is double the value of LMO and LMO-Pt. Comparing the results from Tables 2 and 3, it can be seen that the presence of oxygen doubles the capacitance of the double layer. The values are even higher if the material is more active towards ORR. This is reasonable since adsorbed oxygen-containing species occupy some space in a double layer.

Figure 5 shows that galvanostatic EIS gives a more reliable and accurate response in comparison to potentiostatic conditions (data not shown; there were difficulties in recording low-frequency responses). However, GEIS requires a large amplitude of currents, which can provoke a considerable impact on the nonlinear response. In order to check the influence of higher harmonics on the apparently linear response of investigated electrode materials, GEIS was recorded for La_2O_3, MnO_2, LMO, and LMO-Pt in O_2-saturated 0.10 M KOH at OCP with a current amplitude of 0.510 mA cm^{-2}. This should induce the changes in potential output in a much wider range (and reasonably the widest) with respect to the GEIS measurements presented in Figure 5, and consequently a nonlinear muti-harmonic response. Since EIS theory is based on the linear response of the first harmonic, its value should be negligibly affected by the intensity of the third harmonic [29,30]. The modulus of the third harmonic of ORR on the investigated electrode material is analyzed and presented in Figure 6.

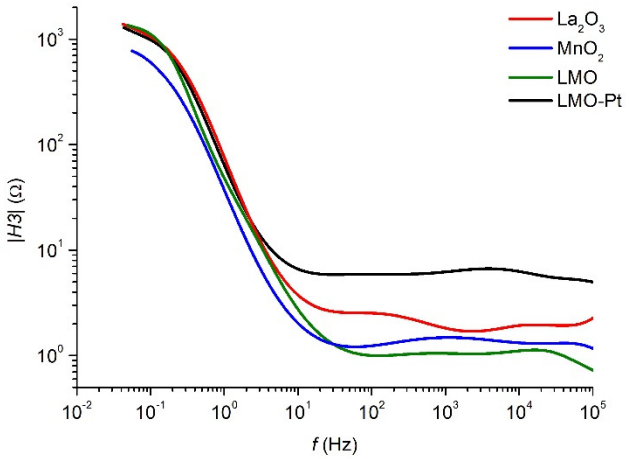

Figure 6. Third harmonics for ORR at La_2O_3, MnO_2, LMO, and LMO-Pt in O_2-saturated 0.10 M KOH gained by GEIS at OCP with current amplitude of 0.10 mA.

At higher frequencies (from 10 Hz to 100 kHz), the intensity of the third harmonic is weakly dependent on frequency, with LMO-Pt showing the most pronounced nonlinearity, followed by La_2O_3, MnO_2, and LMO. At lower frequencies, the nonlinearity contributes gradually more due to diffusion impact. The MnO_2 electrode material is of the lowest intensity of the third harmonic in the low-frequency domain, while the intensities of La_2O_3 and LMO increase to approach the intensity of LMO-Pt. Registered spectra of the third harmonic indicate that diffusion contributes much more to the nonlinearity than charge transfer does, whereas the increased number of components in the catalyst induces the nonlinearity of the charge transfer process. Combining the data for the activity from Table 3 (R2, activity series, as follows: LMO $\approx$ MnO_2 > LMO-Pt >> La_2O_3) and those for CP1-T from Table 2 as a measure of active surface area (LMO-Pt > La_2O_3 > MnO_2 > LMO), it can be concluded that Figure 6 clearly shows that the most ORR active samples, LMO and MnO_2, are of the least expressed charge transfer nonlinearity. This also holds to a less pronounced extent for the region of diffusion control at low frequencies.

The influence of the third harmonic on the first is illustrated in Figure 7 for the LMO-Pt sample, which showed the highest intensities of the third harmonic. The third harmonic starts increasingly to influence the output at the frequencies below 1 Hz and reaches almost 20% of the complete output intensity at the lowest applied frequency. This indicates that the output intensity should be corrected for the contribution of the third harmonic to gain reliable GEIS data related to linear response. The impedance complex plane plots with the contribution of the third harmonic to the output excluded are shown in Figure 7. Loop-like dependences are obtained, which appear more or less elongated, depending on the sample, in the direction of increasing the imaginary impedance. This behavior could be associated with the inductive contribution, which is usually attributed to the adsorption phenomena in the ORR mechanism expressed in the low-frequency domain [31]. Figure 7 shows that more pronounced elongations are found for La-containing samples. This introduces La_2O_3 as the catalyst component that affects mostly the adsorption steps in the ORR mechanism and consequently facilitates the spill-over issues.

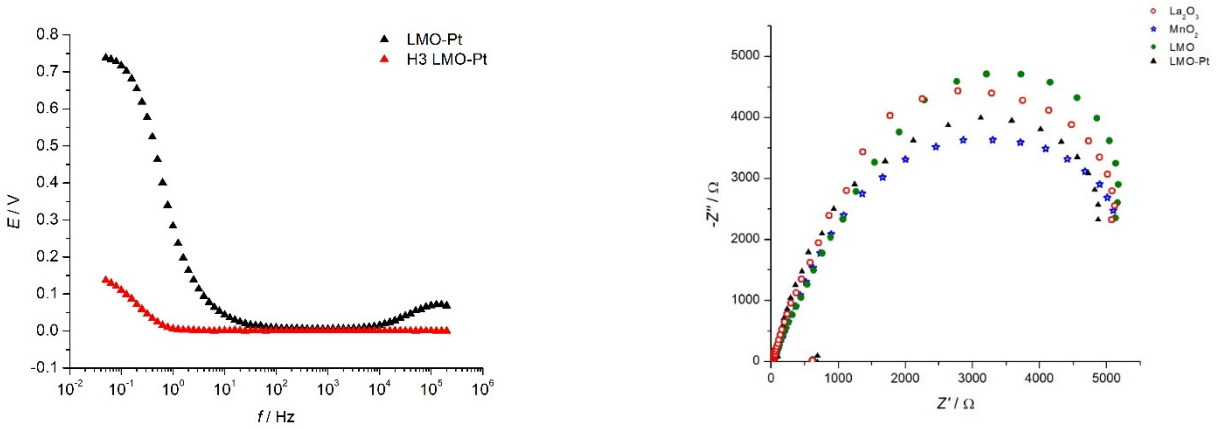

(**a**) (**b**)

Figure 7. (**a**) First and third harmonic for LMO-Pt electrode material and (**b**) Adjusted Nyquist diagrams of La_2O_3, MnO_2, LMO, and LMO-Pt electrolytic material in O_2-saturated 0.10 M KOH at currents that correspond to OCP.

3. Materials and Methods

3.1. Synthesis

The synthesis of MnO_2 was performed by mixing equimolar concentrations of commercial $KMnO_4$ and $MnCl_2$. The equimolar concentration was determinate via oxidation equation 2 $KMnO_4$ (aq) + 2 $MnCl_2$ (aq) → 4 MnO_2 (s) + 2 KCl (aq) + Cl_2 (g). The mixture was heated to 80 °C during 30 min with constant mixing.

LMO was prepared by mixing starting precursor solutions to give desired stoichiometric mole ratios La:Mn = 2:5. Commercial La_2O_3 and $KMnO_4$ were used in such concentrations that they give mentioned La:Mn mole ratios. The chemicals were mixed with reflux and constant mixing at 100 °C during 3 h.

Preparation of LMO-Pt was conducted by mixing La_2O_3 and $KMnO_4$ so that mole ratios would be La:Mn = 2:5 with the addition of 5 mass% H_2PtCl_4. The mixture was subsequently heated to 100 °C with reflux and constant mixing during 24 h.

All the chemicals used were commercial Sigma-Aldrich (Saint Louis, MO, USA) P.A.

3.2. Electrochemical Characterization

Electrochemical behavior was analyzed by cyclic voltammetry, linear sweep voltammetry, potentiostatic electrochemical impedance spectroscopy (PEIS), and galvanostatic electrochemical impedance spectroscopy (GEIS). Measurements were performed by three-electrode cell system in 0.1 M solution of KOH. Counter and reference electrodes were platinum wire and Hg | Hg_2Cl_2, respectively. Working electrode was prepared by putting 30 µL of desired solution on glassy carbon. The electrode ink solution was prepared by mixing the powder with ultrapure double distilled water at a concentration of 5 mg/mL. After 2 h of drying in the air atmosphere, the electrodes were covered with 20 µL of Nafion solution (in water, the ratio 1:100), and dried for 2 more hours. Before the CV and PEIS measurements, the electrolyte was purged with N_2 for 30 min. Prior to LSV and GEIS measurements, the electrolyte was saturated with O_2. For electrochemical measurements potentiostat/galvanostat (BioLogic SAS, SP-240, Grenoble, France) was used. CV measurements were conducted at scan rate of 50 mVs^{-1} between the potentials of −0.2 and 1.7 V vs. RHE at room temperature. PEIS measurements were conducted at open circuit potentials. LSV scan rate was 2 mVs^{-1} and electrode rotating rate was 1000 rpm. GEIS measurements were taken at current densities of −0.765 mA cm^{-2} with an amplitude of 0.510 mA cm^{-2}. The same measuring parameters were used for all the samples. All the measurements in the experiments are presented vs. RHE.

4. Conclusions

Electrocatalytic materials based on metal oxides, La_2O_3, and MnO_2 were synthesized and tested for their activity for oxygen reduction reaction (ORR).

The behavior in ORR indicated that La_2O_3 is of different ORR kinetics with respect to MnO_2, La_2O_3/MnO_2 (LMO), and LMO-Pt electrode materials. The investigation indicates that the surface adsorption of the oxygen species is most likely the rate-determining step for ORR. La_2O_3 has the highest activity towards ORR at low overpotentials, but it reaches the lowest limiting currents, while MnO_2, LMO, and LMO-Pt electrolytic materials have similar activity for ORR.

The capacitance is considerably increased by Pt incorporation into the oxide mixture. MnO_2 and La_2O_3-containing materials exhibit competitive contributions of redox transitions of Mn and pore resistance, depending on the composition. The capacitive response can be governed by Pt, which could appear much to populate the surface of oxide particles rather than the opposite.

Charge transfer resistance indicated the ORR activity series LMO $\approx$ MnO_2 > LMO-Pt >> La_2O_3, with the oxide material showing the highest activity due to the interactive role of La oxide. The molar activity of Mn oxide is found to be doubled by interactivity. The introduction of a small amount of Pt was not found to considerably affect the ORR kinetics of oxides.

Author Contributions: S.V.P.: Investigation, data curation, methodology. M.R.P.P.: Conceptualization, validation, visualization, writing-original draft, writing-review. M.M.V.: Formal analysis, writing-original draft, writing–review. V.T.: Data curation. S.S.: Conceptualization. B.F.: Funding acquisition. M.M.P.: Supervision, visualization, writing-original draft, writing–review. All authors have read and agreed to the published version of the manuscript.

Funding: This work was supported by the Ministry of Education, Science and Technological Development of the Republic of Serbia (Grant No. 451-03-68/2022-14/200026). The authors would like to thank the Ministry of Education, Science and Technological Development of the Republic of Serbia and DAAD, Germany, for funding of the Project No.: 57334757.

Data Availability Statement: All available data are contained within the article.

Acknowledgments: The authors would like to thank Vladimir Panić and Jasmina Stevanović for help in results analysis.

Conflicts of Interest: The authors declare that they have no known competing financial interest or personal relationships that could have appeared to influence the work reported in this paper.

Sample Availability: Samples of the La_2O_3, MnO_2, LMO, and LMO–Pt powders are available from the authors.

References

1. Wang, X.; Li, Z.; Qu, Y.; Yuan, T.; Wang, W.; Wu, Y.; Li, Y. Review of Metal Catalysts for Oxygen Reduction Reaction: From Nanoscale Engineering to Atomic Design. *Chem* **2019**, *5*, 1486–1511. [CrossRef]
2. Li, Z.; Yang, Y.; Relefors, A.; Kong, X.; Siso, G.M.; Wickman, B.; Kiros, Y.; Soroka, I.L. Tuning morphology, composition and oxygen reduction reaction (ORR) catalytic performance of manganese oxide particles fabricated by γ-radiation induced synthesis. *J. Colloid Interface Sci.* **2021**, *583*, 71–79. [CrossRef]
3. Kodama, K.; Nagai, T.; Kuwaki, A.; Jinnouchi, R.; Morimoto, Y. Challenges in applying highly active Pt-based nanostructured catalysts for oxygen reduction reactions to fuel cell vehicles. *Nat. Nanotechnol.* **2021**, *16*, 140–147. [CrossRef] [PubMed]
4. Ren, X.; Lv, Q.; Liu, L.; Liu, B.; Wang, Y.; Liu, A.; Wu, G. Current progress of Pt and Pt-based electrocatalysts used for fuel cells. *Sustain. Energy Fuels* **2020**, *4*, 15–30. [CrossRef]
5. Wang, Y.; Li, J.; Wei, Z. Transition-metal-oxide-based catalysts for the oxygen reduction reaction. *J. Mater. Chem. A* **2018**, *6*, 8194–8209. [CrossRef]
6. Che, H.; Lv, Y.; Liu, A.; Mu, J.; Zhang, X.; Bai, Y. Facile synthesis of three dimensional flower-like Co3O4@MnO2 core-shell microspheres as high-performance electrode materials for supercapacitors. *Ceram. Int.* **2017**, *43*, 6054–6062. [CrossRef]
7. Dessie, Y.; Tadesse, S.; Eswaramoorthy, R.; Abebe, B. Recent developments in manganese oxide based nanomaterials with oxygen reduction reaction functionalities for energy conversion and storage applications: A review. *J. Sci. Adv. Mater. Devices* **2019**, *4*, 353–369. [CrossRef]

8. Neburchilov, V.; Wang, H.; Martin, J.J.; Qu, W. A review on air cathodes for zinc–air fuel cells. *J. Power Sources* **2010**, *195*, 1271–1291. [CrossRef]
9. Lv, J.; Zhang, Y.; Lv, Z.; Huang, X.; Wang, Z.; Zhu, X.; Wei, B. Strontium doped lanthanum manganite (LSM) effects on electrochemical performance of LSM/MnO2 composites for supercapacitor. *J. Mater. Sci. Mater. Electron.* **2017**, *28*, 17020–17025. [CrossRef]
10. Xia, H.; Zhu, D.; Luo, Z.; Yu, Y.; Shi, X.; Yuan, G.; Xie, J. Hierarchically Structured Co3O4@Pt@MnO2 Nanowire Arrays for High-Performance Supercapacitors. *Sci. Rep.* **2013**, *3*, 2978. [CrossRef]
11. Lahousse, C.; Bernier, A.; Grange, P.; Delmon, B.; Papaefthimiou, P.; Ioannides, T.; Verykios, X. Evaluation of gamma-MnO2 as a VOC removal catalyst: Comparison with a noble metal catalyst. *J. Catal.* **1998**, *178*, 214–225. [CrossRef]
12. Zhang, T.; Ge, X.; Zhang, Z.; Tham, N.N.; Liu, Z.; Fisher, A.; Lee, J.Y. Improving the Electrochemical Oxygen Reduction Activity of Manganese Oxide Nanosheets with Sulfurization-Induced Nanopores. *ChemCatChem* **2018**, *10*, 422–429. [CrossRef]
13. Huang, M.; Zhang, Y.; Li, F.; Wang, Z.; Alamusi; Hu, N.; Wen, Z.; Liu, Q. Merging of Kirkendall Growth and Ostwald Ripening: CuO@MnO2 Core-shell Architectures for Asymmetric Supercapacitors. *Sci. Rep.* **2014**, *4*, 4518. [CrossRef] [PubMed]
14. Li, Y.; Peng, H.; Zhang, C.; Chu, M.; Xiao, P.; Zhang, Y. Branched ultra-fine nickel oxide/manganese dioxide core–shell nanosheet arrays for electrochemical capacitors. *RSC Adv.* **2015**, *5*, 77115–77121. [CrossRef]
15. Zhang, X.; Xiao, Q.; Zhang, Y.; Jiang, X.; Yang, Z.; Xue, Y.; Yan, Y.-M.; Sun, K. La2O3 Doped Carbonaceous Microspheres: A Novel Bifunctional Electrocatalyst for Oxygen Reduction and Evolution Reactions with Ultrahigh Mass Activity. *J. Phys. Chem. C* **2014**, *118*, 20229–20237. [CrossRef]
16. Badawy, A.; Ibrahim, S.M.I. The influence of La2O3-doping on structural, surface and catalytic properties of nano-sized cobalt–manganese mixed oxides. *Int. J. Ind. Chem.* **2016**, *7*, 287–296. [CrossRef]
17. Wang, N.; Liu, J.; Gu, W.; Song, Y.; Wang, F. Toward Synergy of Carbon and La 2 O 3 in Their Hybrid as Efficient Catalyst for Oxygen Reduction Reaction. *RSC Adv.* **2016**, *6*, 77786–77795. [CrossRef]
18. Sunarso, J.; Torriero, A.A.J.; Zhou, W.; Howlett, P.C.; Forsyth, M. Oxygen Reduction Reaction Activity of La-Based Perovskite Oxides in Alkaline Medium: A Thin-Film Rotating Ring-Disk Electrode Study. *J. Phys. Chem. C* **2012**, *116*, 5827–5834. [CrossRef]
19. Zhu, H.; Zhang, P.; Dai, S. Recent Advances of Lanthanum-Based Perovskite Oxides for Catalysis. *ACS Catal.* **2015**, *5*, 6370–6385. [CrossRef]
20. Chen, D.; Chen, C.; Baiyee, Z.M.; Shao, Z.; Ciucci, F. Nonstoichiometric Oxides as Low-Cost and Highly-Efficient Oxygen Reduction/Evolution Catalysts for Low-Temperature Electrochemical Devices. *Chem. Rev.* **2015**, *115*, 9869–9921. [CrossRef]
21. Paulraj, A.R.; Kiros, Y. La0.1Ca0.9MnO3/Co3O4 for oxygen reduction and evolution reactions (ORER) in alkaline electrolyte. *J. Solid State Electrochem.* **2018**, *22*, 1697–1710. [CrossRef]
22. Shafi, P.M.; Joseph, N.; Thirumurugan, A.; Bose, A. Enhanced Electrochemical Performances of Agglomeration-free LaMnO 3 Perovskite Nanoparticles and Achieving High Energy and Power Densities with Symmetric Supercapacitor Design. *Chem. Eng. J.* **2018**, *338*, 147–156. [CrossRef]
23. Varničić, M.; Pavlović, M.M.; Eraković Pantović, S.; Mihailović, M.; Pantović Pavlović, M.R.; Stopić, S.; Friedrich, B. Spray-Pyrolytic Tunable Structures of Mn Oxides-Based Composites for Electrocatalytic Activity Improvement in Oxygen Reduction. *Metals* **2022**, *12*, 22. [CrossRef]
24. Fink, M.; Eckhardt, J.; Khadke, P.; Gerdes, T.; Roth, C. Bifunctional α-MnO_2 and Co_3O_4 Catalyst for Oxygen Electrocatalysis in Alkaline Solution. *ChemElectroChem* **2020**, *7*, 4822–4836. [CrossRef]
25. Shinagawa, T.; Garcia-Esparza, A.T.; Takanabe, K. Insight on Tafel slopes from a microkinetic analysis of aqueous electrocatalysis for energy conversion. *Sci. Rep.* **2015**, *5*, 13801. [CrossRef]
26. Marković, N.; Schmidt, T.; Stamenkovic, V.; Ross, P. Oxygen Reduction Reaction on Pt and Pt Bimetallic Surfaces: A Selective Review. *Fuel Cells J.* **2001**, *1*, 105–116. [CrossRef]
27. Eraković, S.; Pavlović, M.M.; Stopić, S.; Stevanović, J.; Mitrić, M.; Friedrich, B.; Panić, V. Interactive promotion of supercapacitance of rare earth/CoO3-based spray pyrolytic perovskite microspheres hosting the hydrothermal ruthenium oxide. *Electrochim. Acta* **2019**, *321*, 134721. [CrossRef]
28. Pavlović, M.M.; Pantović Pavlović, M.R.; Eraković Pantović, S.G.; Stevanović, J.S.; Stopić, S.R.; Friedrich, B.; Panić, V.V. The Roles of Constituting Oxides in Rare-Earth Cobaltite-Based Perovskites on their Pseudocapacitive Behavior. *J. Electroanal. Chem.* **2021**, *897*, 115556. [CrossRef]
29. Weiner, D.D.; Spina, J.F. *Sinusoidal Analysis and Modeling of Weakly Nonlinear Circuits: With Application to Nonlinear Interference Effects*; Van Nostrand Reinhold Company: New York, NY, USA, 1980.
30. Bensmann, B.; Petkovska, M.; Vidaković-Koch, T.; Hanke-Rauschenbach, R.; Sundmacher, K. Nonlinear Frequency Response of Electrochemical Methanol Oxidation Kinetics: A Theoretical Analysis. *J. Electrochem. Soc.* **2010**, *157*, B1279. [CrossRef]
31. Singh, R.K.; Devivaraprasad, R.; Kar, T.; Chakraborty, A.K.; Neergat, M. Electrochemical Impedance Spectroscopy of Oxygen Reduction Reaction (ORR) in a Rotating Disk Electrode Configuration: Effect of Ionomer Content and Carbon-Support. *J. Electrochem. Soc.* **2015**, *162*, F489. [CrossRef]